

Orientation dependent elastic stress concentration at tips of slender objects translating in viscoelastic fluids

Chuanbin Li^b, Becca Thomases^a, and Robert D. Guy^a

^aDepartment of Mathematics, University of California Davis, Davis, CA 95616

^bDepartment of Mathematics, The Pennsylvania State University, University Park, PA 16802

February 25, 2019

Abstract

Elastic stress concentration at tips of long slender objects moving in viscoelastic fluids has been observed in numerical simulations, but despite the prevalence of flagellated motion in complex fluids in many biological functions, the physics of stress accumulation near tips has not been analyzed. Here we theoretically investigate elastic stress development at tips of slender objects by computing the leading order viscoelastic correction to the equilibrium viscous flow around long cylinders, using the weak-coupling limit. In this limit nonlinearities in the fluid are retained allowing us to study the biologically relevant parameter regime of high Weissenberg number. We calculate a stretch rate from the viscous flow around cylinders to predict when large elastic stress develops at tips, find thresholds for large stress development depending on orientation, and calculate greater stress accumulation near tips of cylinders oriented parallel to motion over perpendicular.

1 Introduction

The interaction of slender objects such as cilia and flagella with surrounding viscoelastic fluid environments occurs in many important biological functions such as sperm swimming in mucus during fertilization and mucus clearance in the lungs. There has been much work devoted to understanding the effect of fluid elasticity in such systems including biological and physical experiments [42, 34, 13, 38], asymptotic analysis for infinite-length swimmers [5, 17, 14, 15, 29, 16, 10, 40, 12], and numerical simulations of finite-length swimmers [45, 43, 46, 41, 47, 32]. While flows around slender finite-length objects are essential to our understanding of the physics of micro-organism locomotion, our understanding of these flows in viscoelastic fluids is limited. Previous experimental and theoretical results have focused largely on sedimentation of slender particles in the limit of vanishing relaxation time, i.e. the low Weissenberg number limit [31, 28, 6, 26, 23, 18, 9].

Numerical simulations of flagellated swimmers in viscoelastic fluids have shown the concentration of polymer elastic stress at the tips of slender objects [45, 46, 47, 32], (see Fig. 1) but why the stress concentrates so strongly at tips, and the effect of these stresses on micro-organism locomotion is not understood. Unlike asymptotic theory [14, 15, 29, 16, 40, 12] these simulations involve large amplitude motions of finite length objects, and these large elastic stresses that arise have a substantially different effect on swimming motion than predicted by asymptotic analysis

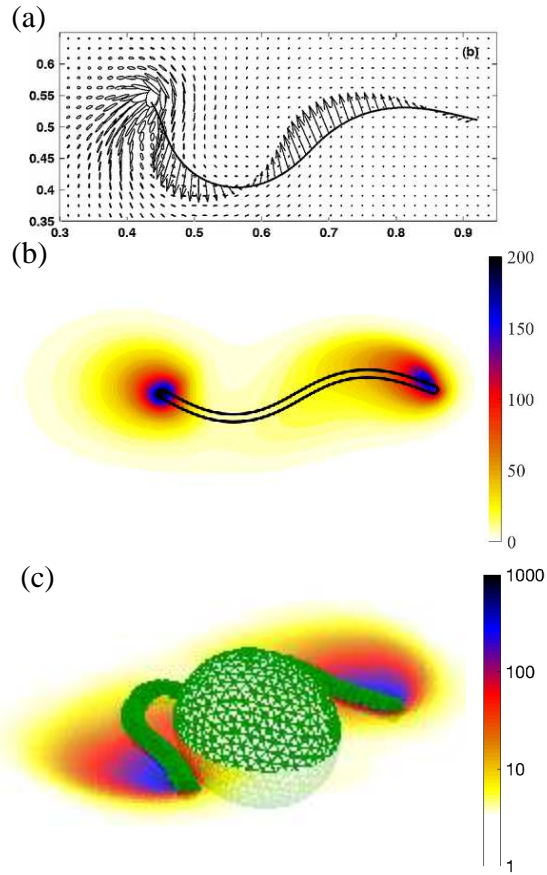


Figure 1: (a) 2D flow around large amplitude, finite-length undulatory swimmer, ellipses show size and orientation of stress concentrated at tail (reproduced from [45]). (b) 2D flow around bending sheet, color field shows strain energy density concentrated at tips. (c) 3D flow around swimming bi-flagellated cell, color field in center plane shows strain energy density.

[47]. Experiments can measure kinematic changes [42, 38], but not elastic stress, and thus the mechanisms of observed behavioral responses cannot be explained by experiments alone.

It was observed in simulations [32] that the concentrated tip stresses are stronger for a cylinder moving parallel to its axis compared to a cylinder moving perpendicular to its axis. This orientation dependence of elastic stress at tips is reversed from the orientation dependence of force on velocity in resistive force theory and related viscous fluid theories [20, 19, 27, 33, 24, 25] which form the basis of much of our intuition about micro-organism locomotion without inertia. Classical viscous theories do not include tip effects, but previous results in viscoelastic fluids [45, 46, 47, 32] suggest that the tip has a special role in the elastic stress development which has not been previously analyzed.

Previous work on the flow of viscoelastic fluids around slender objects has been done in the weakly nonlinear (or low Weissenberg number, Wi) regime [31, 28, 6, 26, 23, 18, 9], but the large stress concentration at tips of thin objects is a nonlinear effect and thus cannot be captured in a low Wi expansion. However, the highly nonlinear regime is challenging for numerical simulations [53], and this has limited the ability to probe dynamics in this regime. As another approach, one can consider the limit of low polymer concentration, decoupling the stress and velocity. This method has been used to study stress localization for high- Wi at extensional points and around objects [54, 50, 51, 57, 56].

The weak coupling expansion, a formal asymptotic approximation in the limit of low polymer concentration, retains viscoelastic nonlinearities at leading order [36]. This method has been successful in capturing high Wi effects for flow around a sphere in 3D [36], and in the study of the rheology of dilute suspensions in the low polymer concentration limit [52]. Similar stress localization in the wake of spheres has been observed experimentally [1, 3] and theoretical predictions of shear thickening for strongly elastic dilute suspensions were in agreement with experimental observations [55].

Here we use the weak coupling expansion to study the equilibrium flow around, and resultant force on, cylinders translating either perpendicular, or parallel to the direction of motion, in a 3D viscoelastic fluid. Using this analysis we explain the origin of the tip stresses, we predict a critical Weissenberg number for the flow transition based on viscous flow data, and we show how the tip stress accumulation depends on cylinder orientation.

2 Model Equations

We examine the viscoelastic fluid flow around a stationary finite-length cylinder of radius a with hemispherical caps driven by a fixed flow at infinity, \mathbf{U}_∞ . We use the Oldroyd-B model of a viscoelastic fluid at zero Reynolds number, which is attractive as a frame-invariant, nonlinear, continuum model of a viscoelastic fluid that can capture the dominant effects of fluid elasticity, e.g. storage of history of deformation on a characteristic time-scale. The dimensionless system of equations is given by

$$\Delta \mathbf{u} - \nabla p + \beta \nabla \cdot \mathbf{C} = 0, \quad (1)$$

$$\nabla \cdot \mathbf{u} = 0, \quad (2)$$

$$\mathcal{D}_t[\mathbf{u}]\mathbf{C} = Wi^{-1}\mathbf{I} + (\nabla \mathbf{u}\mathbf{C} + \mathbf{C}\nabla \mathbf{u}^T) - Wi^{-1}\mathbf{C}, \quad (3)$$

for \mathbf{u} the fluid velocity, p the fluid pressure, and \mathbf{C} , the conformation tensor, a macroscopic average of the polymer orientation and stretching that is related to the polymer stress tensor by $\boldsymbol{\sigma}^p = \beta(\mathbf{C} - \mathbf{I})$. We use $\mathcal{D}_t[\mathbf{u}]$ to denote the material time derivative along the velocity field \mathbf{u} . The

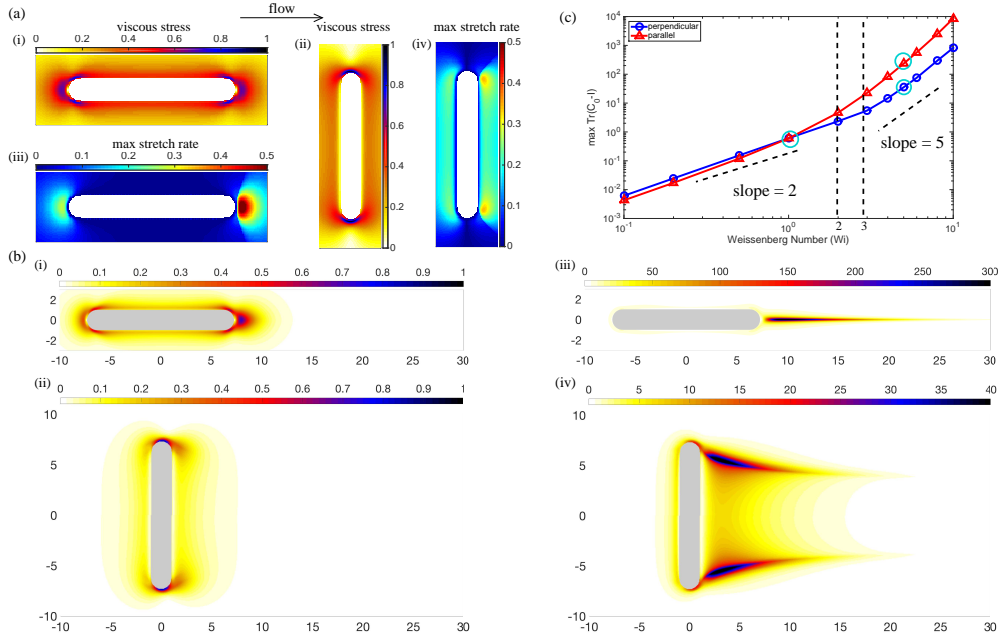


Figure 2: (a) Norm of viscous stress in the center plane for cylinders oriented (i) parallel ($\max \|2\mathbf{D}_0^{\parallel}\| \approx 0.78$) and (ii) perpendicular ($\max \|2\mathbf{D}_0^{\perp}\| \approx 0.95$) to flow; stretch rates of viscous flow for cylinders oriented (iii) parallel ($\max \nu^{\parallel} \approx 0.5$) and (iv) perpendicular ($\max \nu^{\perp} \approx 0.34$) to flow. Flow goes from left to right. (b) $\text{Tr}(\mathbf{C}_0 - \mathbf{I})$ in the center plane for cylinders with (i)-(ii) $Wi = 1$ and (iii)-(iv) $Wi = 5$ (note the difference in scale). (c) Maximum of $\text{Tr}(\mathbf{C}_0 - \mathbf{I})$ as a function of Wi for the two orientations, in log scales. Dotted lines show the two critical Weissenberg numbers $Wi \approx 2$, and $Wi \approx 3$, cyan circles indicate Wi values pictured in (b).

parameters, β , the non-dimensional polymer stiffness, and Wi , the Weissenberg number, or non-dimensional relaxation time, are defined by

$$\beta = \frac{Gr}{\mu U}, \quad Wi = \frac{\lambda U}{r}, \quad (4)$$

for μ the fluid viscosity, λ the fluid relaxation time, G the polymer elastic modulus, and $U = |\mathbf{U}_\infty|$.

The force on a stationary cylinder in a background flow is proportional to the rate at which energy is dissipated by the fluid. To calculate the dissipation rate we integrate the dot product of $(\mathbf{u} - \mathbf{U}_\infty)$ and Eq. (1) over the fluid domain, Ω (exterior to the cylinder). After some manipulations and using the incompressibility constraint we obtain

$$\mathbf{U}_\infty \cdot \mathbf{F} = 2 \int_{\Omega} D_{ij} D_{ij} dV + \beta \int_{\Omega} \frac{\partial u_i}{\partial x_j} C_{ij} dV, \quad (5)$$

where $D_{ij} = \frac{1}{2} \left(\frac{\partial u_i}{\partial x_j} + \frac{\partial u_j}{\partial x_i} \right)$ is the rate of strain tensor, $\mathbf{F} = \int_{\partial\Omega} (\boldsymbol{\sigma}^n + \beta \mathbf{C}) \cdot \mathbf{n} dS$ is the force on the cylinder, and $\boldsymbol{\sigma}^n = 2\mathbf{D} - p\mathbf{I}$ is the Newtonian stress tensor. Thus for a constant velocity at infinity the force on the cylinder is proportional to the sum of the viscous dissipation rate and the rate at which energy is transferred to the polymers.

The polymer strain energy is $\mathcal{E} = \int_{\Omega} \text{Tr}(\mathbf{C} - \mathbf{I}) dV$ [4], and an equation for the strain energy is obtained by taking the trace of Eq. (3) and integrating over the fluid domain,

$$\frac{d}{dt} \mathcal{E} = 2 \int_{\Omega} \frac{\partial u_i}{\partial x_j} C_{ij} dV - Wi^{-1} \mathcal{E}. \quad (6)$$

Changes in the polymer energy come from transfer of energy between the fluid and the polymer and energy lost to polymer relaxation. Therefore at steady state the rate of energy loss to the fluid is proportional to the polymer energy. By combining Eq. (5) with Eq. (6) one finds that at steady state the force on the cylinder is

$$\mathbf{U}_\infty \cdot \mathbf{F} = 2 \int_{\Omega} D_{ij} D_{ij} dV + \frac{\beta}{2Wi} \mathcal{E}. \quad (7)$$

Hence the strain energy \mathcal{E} quantifies the force on the cylinder due to viscoelasticity.

3 Weak-coupling expansion

Previous theoretical results on the polymeric contribution to a translating cylinder have used a second-order fluid expansion in the weakly nonlinear regime [30, 21, 44, 9, 11], where the nonlinearities associated with viscoelasticity are lost at leading order. We are interested in the regime of large amplitude motions where large stress accumulates in the fluid, so we consider the *weakly coupled*, or small β , regime where the nonlinearities enter at leading order but the coupling between the polymer and fluid is higher order. The weak coupling expansion was introduced for flow around a sphere in [36], and is similar to analysis of viscoelastic fluids using fixed velocity fields in the high Wi regime [39, 48]. Analysis of viscoelastic fluids with fixed velocity fields have predicted transitions in behavior for high Wi at steady extensional points [54, 50, 51, 57, 56] and qualitatively similar transitions are also found in simulations where the velocity and the stress are fully coupled [56].

We expand the solutions in β , $\mathbf{u} \sim \mathbf{u}_0 + \beta \mathbf{u}_1$, $p \sim p_0 + \beta p_1$, and $\mathbf{C} \sim \mathbf{C}_0 + \beta \mathbf{C}_1$. At leading order Eqs. (1)–(2) decouple from Eq. (3), and \mathbf{u}_0 is the solution for the viscous flow around the cylinder. The conformation tensor satisfies

$$\mathcal{D}_t[\mathbf{u}_0]\mathbf{C}_0 = \text{Wi}^{-1}\mathbf{I} + \mathcal{S}[\mathbf{u}_0]\mathbf{C}_0 - \text{Wi}^{-1}\mathbf{C}_0, \quad (8)$$

where $\mathcal{S}[\mathbf{u}_0]\mathbf{C}_0 \equiv (\nabla\mathbf{u}_0\mathbf{C}_0 + \mathbf{C}_0\nabla\mathbf{u}_0^T)$. On a given streamline Eq. 8 is an ODE involving a source term, $\text{Wi}^{-1}\mathbf{I}$, a stretching term, $\mathcal{S}[\mathbf{u}_0]$, and a relaxation term, $\text{Wi}^{-1}\mathbf{C}_0$.

4 Tip stress development

We prescribe a unit flow in the x -direction, $\mathbf{U}_\infty = \mathbf{e}_x$, in the domain exterior to a cylinder that is oriented either parallel or perpendicular to the direction of flow, with no-slip boundary conditions on the cylinder walls. The circular cylinder has length 4π , radius $a = 1$, and is capped at both ends with hemispheres. We solve the Stokes equations for \mathbf{u}_0 using a boundary integral method based on a regularized Green's function from the method of regularized Stokeslets [8]. We generate streamlines of the Newtonian flow \mathbf{u}_0 and evolve Eq. (8) along those streamlines. See supplementary information for more details.

In Fig. (2) (a) we plot the Frobenius norm (defined $\|\mathbf{A}\| \equiv \sqrt{A_{ij}A_{ij}}$) of the leading order viscous stress tensor $2\mathbf{D}_0$ in the center plane for cylinders oriented (i) parallel and (ii) perpendicular to the flow. Note that the viscous stress near the middle of the cylinders is 2 or 3 times smaller than that at the tips. In Fig. 2 (b) we show color fields of the leading order polymer strain energy density $\text{Tr}(\mathbf{C}_0 - \mathbf{I})$, for two different Weissenberg numbers (i)-(ii) $\text{Wi} = 1$ and (iii)-(iv) $\text{Wi} = 5$. For $\text{Wi} = 1$ the elastic stress is concentrated at the tips like the viscous stress, and on the same scale as the viscous stress. For $\text{Wi} = 5$ however, the elastic stress at the tips is more than 100 times larger than for $\text{Wi} = 1$, and concentrated in the wake. This nonlinear response has been seen before in analysis of flow around a circle in 2D [22, 35, 2] and around a sphere in 3D [36]. However, in Fig. 2 (b) (iii)-(iv) we also see that the stress in the wake of the cylinder that is oriented parallel to the direction of the flow is about 10 times larger than that for the cylinder oriented perpendicular to the direction of flow. We examine the Newtonian flow that drives the stress growth to understand what sets the transition in Wi , and how the cylinder orientation impacts stress growth so dramatically for large Wi .

At a fixed point in the flow, the real parts of the eigenvalues of the operator $\mathcal{S}[\mathbf{u}_0]$, defined in Eq. (8), set the growth (or decay) rates of \mathbf{C}_0 due to stretching (or compression). The solution to the eigenvalue problem $\mathcal{S}[\mathbf{u}]\mathbf{C} = \nu\mathbf{C}$ is $\mathbf{C} = \mathbf{v}_i\mathbf{v}_j^T$, $\nu_{ij} = \mu_i + \mu_j$, where μ_i is an eigenvalue of $\nabla\mathbf{u}$ with corresponding eigenvector \mathbf{v}_i . We define the max stretch rate ν at a point as

$$\nu = 2 \max(\text{Re}(\Lambda(\nabla\mathbf{u}_0))), \quad (9)$$

where $\Lambda(A)$ is the set of eigenvalues of the matrix A . In regions of the flow where $\nu - \text{Wi}^{-1} > 0$, or $\nu\text{Wi} > 1$, stretching outpaces relaxation, and while fluid particles remain in these stretching regions they experience unbounded stress growth.

In Fig. 2 (a) we plot ν in the center plane for the cylinder oriented parallel (iii) and the cylinder oriented perpendicular (iv). The maximum stretch rate for both cylinders occurs in the wake of the cylinder, i.e. the max stretch rate contains information about flow directionality that is missing from Fig. (2) (a) (i)-(ii). We see that the cylinder oriented parallel to motion has $\max(\nu^{\parallel}) \approx 0.5$, thus $\text{Wi}^{\parallel} \approx 2$ is a threshold for stretching outpacing relaxation in regions of this flow. The maximum for the perpendicularly oriented cylinder is smaller, $\max(\nu^{\perp}) \approx 0.34$, corresponding to a threshold

$Wi^\perp \approx 3$ for large stress growth. For the perpendicularly oriented cylinder, the flow in the regions of high viscous stress near the tip is locally a shear flow, whereas, the local flow is extensional (which is known to lead to more rapid elastic stress growth [58]) near the tips of the cylinder oriented parallel. The difference in flow type is reflected in the max stretch rate which is largest near the trailing tip of the cylinder oriented parallel to motion where the viscous stress is largest. For the perpendicularly oriented cylinder, the strongest extension is behind the cylinder where the viscous stresses are weaker.

In Fig. 2 (c) we plot $\max \text{Tr}(\mathbf{C}_0 - \mathbf{I})$ for $Wi \leq 10$. For both orientations, the maximum of $\text{Tr}(\mathbf{C}_0 - \mathbf{I})$ scales like Wi^2 below $Wi \approx 2$, and scales like Wi^5 above $Wi \approx 3$. The cylinder oriented parallel to motion has a larger max stretch rate and thus it enters the regime of large stress growth for lower Wi than the perpendicularly oriented cylinder, leading to larger stress for a fixed Wi beyond the threshold $Wi^\parallel \approx 2$. Recall that the contribution to the force from the polymeric stress scales like $\frac{\beta}{2Wi}\mathcal{E}$ and thus for low Wi there is a $\mathcal{O}(Wi)$ contribution to the force whereas for high Wi the contribution is $\mathcal{O}(Wi^4)$. Theoretical results have predicted similar scalings for related problems [39, 48, 36].

5 Viscoelastic correction to force

We expand the force on a cylinder to first order in β as

$$\mathbf{F} \sim \int_{\partial\Omega} \boldsymbol{\sigma}_0^n \cdot \mathbf{n} + \beta (\boldsymbol{\sigma}_1^n + \mathbf{C}_0) \cdot \mathbf{n} dS \equiv \mathbf{F}_0 + \beta \mathbf{F}_1. \quad (10)$$

We avoid computing \mathbf{u}_1 , the first-order correction to the velocity, by using reciprocal relations [30, 21, 44, 9, 11], as has been done before in many calculations of non-Newtonian corrections at low Reynolds number. In addition, because the flow and force are parallel for these orientations, we obtain the magnitude of \mathbf{F}_1 as

$$F_1 = Wi^{-1} \int_{\Omega} \text{Tr}(\mathbf{C}_0 - \mathbf{I}) dV. \quad (11)$$

Details of our calculation are provided in supplementary information. Thus the viscoelastic correction to the force is proportional to the integral of the trace of the leading order polymer stress tensor over the fluid domain.

In Fig. 3 (a) we plot the viscoelastic force correction, F_1 , normalized by $F_0^\perp = 65$ (note $F_0^\parallel = 48$) for $Wi \leq 10$ for each cylinder orientation. We see that in the expansion the $\mathcal{O}(\beta)$ force correction is up to 25 times the viscous force for large Wi . The perpendicular force correction is larger than the parallel force correction, however Fig. 3 (b) shows F_1^\parallel/F_1^\perp (left hand axes) and beyond $Wi \approx 2$ (the parallel stress growth threshold) F_1^\parallel increases more than F_1^\perp , and this continues until about $Wi \approx 6$ where the ratio starts to decrease again. Since we are interested in the ‘‘tip effect’’, we calculate the contribution to the force from a single tip.

We define this tip force by restricting the integration domain in Eq. (11) to a subdomain exterior to the cylinder that contains only one tip. In Fig. 3 (d) we show the tip of the perpendicular cylinder with the strain energy density for $Wi = 5$. We consider a streamline that approaches very close to the tip in the center plane and we evolve the streamline until it levels off for large x , and we define the value it approaches, $y_{\text{tip}} = 3.41$, as shown in Fig. 3 (d). With this we define

$$F_1^{\text{tip}} = Wi^{-1} \int_{\Omega \setminus \{y < y_{\text{tip}}\}} \text{Tr}(\mathbf{C}_0 - \mathbf{I}) dV. \quad (12)$$

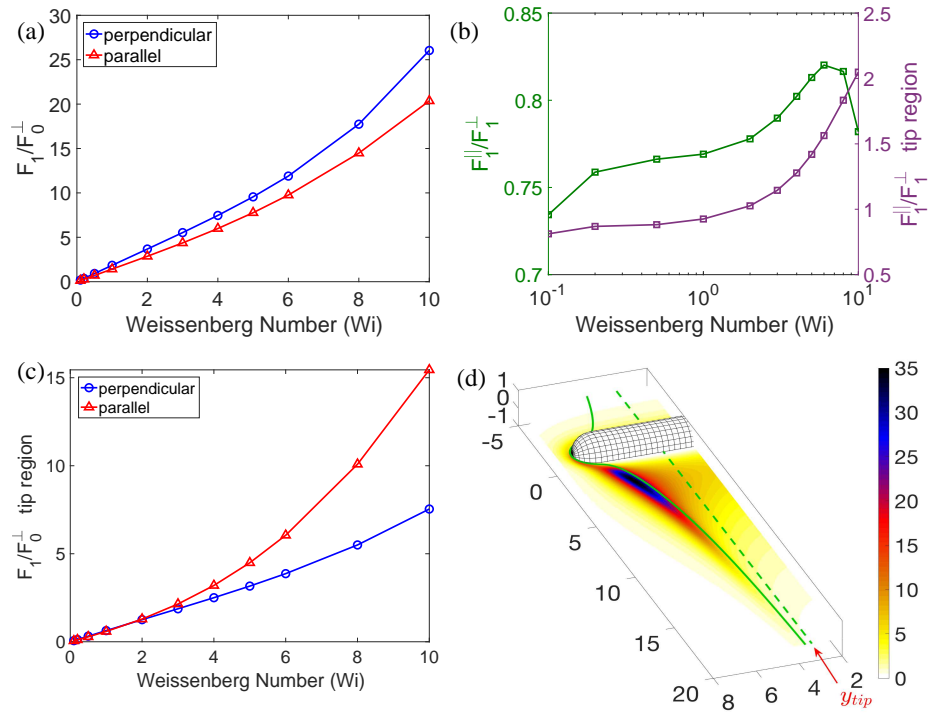


Figure 3: (a) F_1/F_0^\perp (perpendicular and parallel) (b) parallel to perpendicular ratio of F_1 : whole domain (left axes), tip region (right axes) (c) F_1 restricted to tip (perpendicular and parallel) (d) Diagram illustrating definition of y_{tip} .

In Fig. 3 (c) we plot $F_1^{\text{tip}}/F_0^\perp$ for $Wi \leq 10$ for each cylinder orientation, and the ratio of tip force corrections in Fig. 3(b) (right hand axes). Beyond the threshold $Wi^\parallel \approx 2$, the parallel force correction at the tip is larger than the perpendicular force correction, and the parallel force correction is double the perpendicular force correction from the tip at high Wi .

6 Discussion

Using the viscous flow field around cylinders we predict a critical Wi beyond which a large stress “tip effect” occurs, and we find that the critical Wi is orientation dependent. There are larger elastic stresses in the wake of cylinders oriented parallel to the direction of motion compared to cylinders oriented perpendicular to the flow. The flow type (shear or extensional) is orientation dependent and is reflected in the larger max stretch rate for the cylinder oriented parallel. The max stretch rate is defined from the eigenvalues of the operator \mathcal{S} in Eq. (8), and this operator appears in all differential models of viscoelasticity, including models which incorporate additional non-Newtonian effects such as shear-thinning. Hence we conjecture that the transitions we have identified are not specific to the Oldroyd-B model, although quantitative values of stress accumulation beyond the transitions will depend on the model.

We explored other tip shapes and found that varying curvature at the tip did not effect the qualitative results; the max stretch rate was always largest near the tip, and greater for cylinders oriented parallel to the motion. The analysis given used the rod thickness to define the characteristic length scale and hence thinner rods will exhibit large stress growth at a lower relaxation time. Although the tip effect is independent of the length, the relative contribution to the total force from the tip depends on the length, and hence, quantifying the role of the tip effect on locomotion requires more investigation. Nevertheless, based on past numerical simulations of flagellated swimmers, it is clear that this tip effect is significant.

In [32] we observed elastic stress accumulation at flagellar tips in a simulation of a bi-flagellated alga cell swimming using experimentally measured kinematics. The stress accumulation was greater on the return stroke when the flagellar tips were oriented parallel to the direction of motion than when oriented perpendicular to the motion. The steady-state analysis of the tip effect presented here helps explain the physics behind these observations made in [32], but generally details of stroke kinematics, including time-dependence, will effect how stresses develop around flagellated swimmers. We are able to make predictions about critical Weissenberg numbers for steady flows by looking at the max stretch rates, but this tool could be useful for other gaits and even in experimental settings where flow fields are obtainable but location and concentration of stress are not measurable.

The authors thank David Stein for interesting discussions and suggestions on this work. R.D.G. and B.T. were supported in part by NSF Grant No. DMS-1664679.

Supplemental Information for Orientation dependent elastic stress concentration at tips of slender objects translating in viscoelastic fluids

Chuanbin Li, Becca Thomases, and Robert D. Guy

S1 Numerical calculation of the flow and stress

S1.1 Cylinder discretization

The cylinders used in the computations are right circular cylinders of length L and radius 1 with hemispherical caps on both ends. Thus the tip-to-tip distance is $L + 2$. Without loss of generality assume that the long axis is oriented in the x -direction. Let N_θ represent the number of points used to discretize the circumference, and let $\Delta\theta = 2\pi/N_\theta$ be the spacing between the points in the circumferential direction. The axial direction is discretized with $N_x = L/\Delta\theta + 1 = LN_\theta/(2\pi) + 1$ points so that the spacing along the axial direction, Δx , is equal to the point spacing in the circumferential direction. We choose L to be an even multiple of π so that N_x as defined above is an integer. The caps are described in spherical coordinates. The azimuth angle is discretized with the same spacing as the the circumferential angle, i.e. $\Delta\phi = \Delta\theta$.

S1.2 Velocity

We evaluate the velocity using a boundary integral with a regularized kernel. The cylinder is stationary with velocity at ∞ given by $\mathbf{U}_\infty = \mathbf{e}_x$. Using the boundary integral formulation [37] the velocity can be evaluated by

$$u_i(\mathbf{x}) = \delta_{i,1} + \int_{\partial\Omega} G_{i,j}(\mathbf{x}, \mathbf{x}^0) F_j(\mathbf{x}^0) dS(\mathbf{x}^0), \quad (\text{S1})$$

where the integral is over the cylinder surface. Because $\mathbf{u} = 0$ on the cylinder surface, the surface force density, \mathbf{F} , satisfies the integral equation

$$-\delta_{i,1} = \int_{\partial\Omega} G_{i,j}(\mathbf{x}, \mathbf{x}^0) F_j(\mathbf{x}^0) dS(\mathbf{x}^0). \quad (\text{S2})$$

Here $G_{i,j}(\mathbf{x}, \mathbf{x}^0)$ is the free-space Green's function for Stokes equation representing the flow in the i -direction at point \mathbf{x} generated by a unit point force oriented in the j -direction at point \mathbf{x}^0 .

We replace the singular kernels by regularized kernels using the Method of Regularized Stokeslets [7, 8]. The discretized and regularized versions of equations (S1) and (S2) are, respectively

$$u_i(\mathbf{x}) = \delta_{i,1} + \frac{1}{8\pi\mu} \sum_k S_{i,j}^\epsilon(\mathbf{x}, \mathbf{x}_k) F_j(\mathbf{x}_k) dA_k, \quad (\text{S3})$$

and

$$-\delta_{i,1} = \frac{1}{8\pi\mu} \sum_k S_{i,j}^\epsilon(\mathbf{x}_n, \mathbf{x}_k) F_j(\mathbf{x}_k) dA_k, \quad (\text{S4})$$

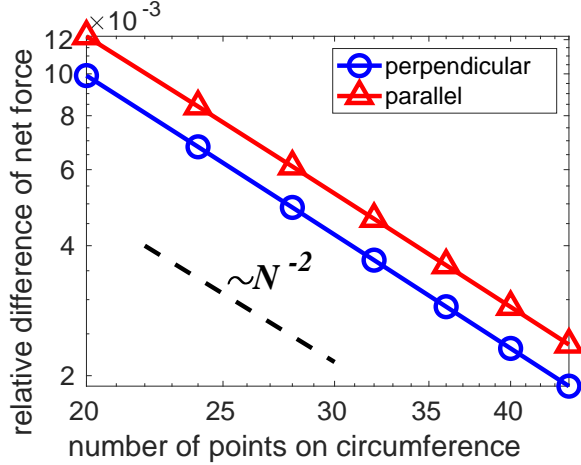


Figure S1: Refinement study for the magnitude of the viscous force on the cylinder as the number of points on the circumference increases.

where \mathbf{x}_n and \mathbf{x}_k are points on the discretized cylinder. We use the form of the regularized Stokeslet from [8], which is

$$S_{i,j}^\epsilon(\mathbf{x}, \mathbf{x}^0) = \delta_{i,j} \frac{r^2 + 2\epsilon^2}{(r^2 + \epsilon^2)^{3/2}} + \frac{(x_i - x_i^0)(x_j - x_j^0)}{(r^2 + \epsilon^2)^{3/2}}, \quad (\text{S5})$$

where $r = \sqrt{(x_i - x_i^0)(x_i - x_i^0)}$. We set $\epsilon = 1.2\Delta x$, where Δx is the point spacing along along the cylinder in the axial direction, and the viscosity is set to 1 from the nondimensionalization.

In Figure S1 we show the results of a refinement study for the magnitude of the viscous force as the number of points on the circumference of the cylinder is refined. The plot shows that the method converges at second-order in the point spacing along the cylinder. The computations in the paper were performed with at least 24 points on the cylinder circumference. The error in the force is estimated to be on the order of 1% at this resolution using the relative difference of the force between successive meshes as an estimate of the error.

S1.3 Conformation tensor

We identify streamlines by integrating the velocity field with a relative error tolerance of 10^{-4} . Along each streamline we compute the velocity gradient using a second-order centered finite-difference with points spaced 10^{-6} in each direction off the streamline. In the weak coupling limit, the polymer stress decouples from the flow, and so the conformation tensor is computed from a known velocity gradient at each order in β . On a given streamline, $\mathbf{X}(t)$, the the equation for the conformation tensor reduces to an ODE, which at leading order is

$$\frac{d\mathbf{C}_0}{dt} = \text{Wi}^{-1}\mathbf{I} + (\nabla\mathbf{u}_0(\mathbf{X}(t))\mathbf{C}_0 + \mathbf{C}_0\nabla\mathbf{u}_0^T(\mathbf{X}(t))) - \text{Wi}^{-1}\mathbf{C}_0. \quad (\text{S6})$$

We use cubic splines to represent the velocity gradients along the streamline, and we integrate this ODE on each streamline with a relative tolerance of 10^{-4} . The conformation tensor is initialized to the identity tensor at the upstream boundary of the computational domain.

S1.4 Integral of the trace of the stress

We compute the solution in a $[-50, 50]^3$ box, but for each orientation, we exploit the appropriate symmetry. The velocity gradient decays like r^{-2} , and the viscous dissipation rate density decays like r^{-4} . The viscous force on the cylinder is the integral of the dissipation rate over the exterior of the cylinder. The relative truncation error of using a domain of size R is $\sim R^{-1}$, and so for a box of size 50 we estimate the truncation errors are around 2%.

For the parallel orientation, the solution is axi-symmetric, and so we compute the streamlines and stresses in the half plane $y = 0, z \geq 0$. The starting points for the streamlines are a set of points along the line segment $x = 0, y = 0$ and $z \in (1, 50]$. From these starting points, the streamlines are generated by integrating forward and backward in time until they reach the boundary of the computational box.

The starting positions of the streamlines are spaced more closely near the cylinder surface than far away. The velocity gradients decay proportional to r^{-2} far from the cylinder, and so few points are needed away from the cylinder. Specifically, we use the nonlinear transformation

$$z = (1 - bw)^{-1/b}, \quad (\text{S7})$$

where $b \geq -1$ is a parameter that affects how clustered the points are near the cylinder surface. Larger values of b result in more clustering of points near the cylinder. This transformation maps the interval $[0, w_{max}]$ to $[1, z_{max}]$, where $w_{max} = (1 - z_{max})^{-b}/b$. We choose a uniformly spaced discretization in w , and then use the transformation to define the starting z values. The transformation is defined by the differential equation

$$dz = z^{b+1} dw \quad (\text{S8})$$

$$z(0) = 1. \quad (\text{S9})$$

Thus, the spacing grows as a power law in z increases. For the computations in the manuscript, we use $b = 0.75$ and 36 discrete points. With these parameters, the streamlines closest to the cylinder are spaced about 0.036 apart, which are much more closely spaced than the points along the cylinder. There are 16 points within the first unit of distance and just 5 points within the interval $[10, 50]$.

For the perpendicular orientation we use a similar approach for increasing the streamline spacing away from the cylinder. The axis of the cylinder is aligned in the y -direction. Because of the symmetry, we compute the solution for $y, z \geq 0$. The starting points for identifying streamlines are from the quarter plane $x = 0, y, z \geq 0$. Streamlines are found from integrating forward and backward in time until reaching the boundary of the computational box ($x = \pm 50$). The starting points are located along curves of a fixed distance from the cylinder surface. The spacing between these curves is selected using the same discretization for starting values for the parallel orientation described above. Along each curve, points are chosen to be equally spaced with spacing approximately equal to the spacing between the curves at this distance.

To compute integrals of the stress, we interpolate the stress to a structured mesh. As with the streamline spacing the mesh is finer near the cylinder and coarser away from it. For the parallel orientation case, we begin with spacing in the z -direction on the interval $(1, 50]$ using the same spacing as the starting points for the streamlines. We then add additional points in between any points which are spaced greater than 5 units apart. For $z \in [0, 1]$ we use equally spaced points with approximately the same spacing as the points near $z = 1$. The spacing in the x -direction is uniform with spacing approximately equal to the finest spacing in the z -direction near the cylinder.

For the perpendicular orientation, we use the same mesh for the z -direction. For the y -direction (axial direction) we use uniform spacing from $y = 0$ (center) to $y = 2\pi + 1$ (tip) with the spacing

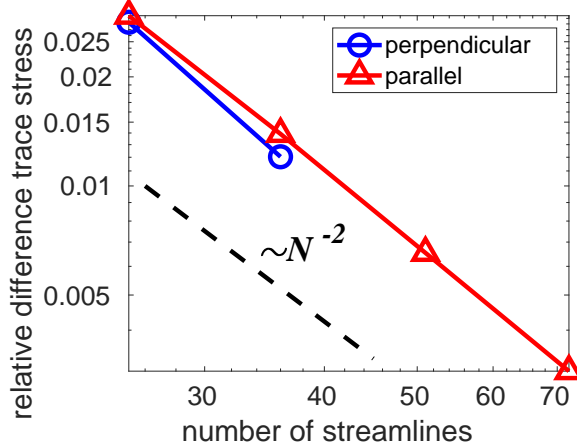


Figure S2: Refinement study for the integral of the trace of the stress for $Wi = 1$ as the number of streamlines used along the z -axis increases. The number of points on the cylinder's circumference is 24 for the perpendicular orientation and 28 for the parallel orientation.

equal to the finest spacing in the z -direction. From the tip to the computational boundary, we use the same stretched grid described previously. In the region $y \in [2\pi + 1, 50]$ we use the same number of points used in the interval $z \in [1, 50]$. The spacing in the x -direction is uniform with spacing approximately equal to the finest spacing in the z -direction near the cylinder.

After interpolating the stress to the mesh, the stress inside the cylinder is set to zero, and the stress is integrated in the cube $[-50, 50]^3$ using trapezoidal rule. In Figure S2 we show that this method converges at second-order in the spacing between the streamlines. The refinement study was performed by computing differences of the integral of the trace of the stress between successive meshes. We used five meshes for the parallel orientation, and three meshes for the perpendicular orientation. The perpendicular case involves many more points and is much more computationally expensive. In the paper we used 36 streamlines along the z -axis, and based on the refinement study, we estimate that the errors are around 2% at this resolution.

S2 Expression for force at first order

S2.1 Reciprocal relation

Let \mathbf{u} be an incompressible velocity field and $\boldsymbol{\sigma}$ be the associated Newtonian stress tensor. We consider two pairs of velocity and stress: $(\mathbf{u}, \boldsymbol{\sigma})$ and $(\mathbf{u}', \boldsymbol{\sigma}')$.

$$u_i \frac{\partial \sigma'_{ij}}{\partial x_j} = \frac{\partial}{\partial x_j} (u_i \sigma'_{ij}) - \frac{\partial u_i}{\partial x_j} \sigma'_{ij} \quad (\text{S10})$$

$$= \frac{\partial}{\partial x_j} (u_i \sigma'_{ij}) - \frac{\partial u_i}{\partial x_j} \left(-p' \delta_{ij} + \mu \left(\frac{\partial u'_i}{\partial x_j} + \frac{\partial u'_j}{\partial x_i} \right) \right) \quad (\text{S11})$$

$$= \frac{\partial}{\partial x_j} (u_i \sigma'_{ij}) - \mu \frac{\partial u_i}{\partial x_j} \left(\frac{\partial u'_i}{\partial x_j} + \frac{\partial u'_j}{\partial x_i} \right) \quad (\text{S12})$$

Now reversing the primes and subtracting we get

$$u_i \frac{\partial \sigma'_{ij}}{\partial x_j} - u'_i \frac{\partial \sigma_{ij}}{\partial x_j} = \frac{\partial}{\partial x_j} (u_i \sigma'_{ij} - u'_i \sigma_{ij}). \quad (\text{S13})$$

This identity will be the starting point for the manipulations below.

S2.2 Weak coupling expansion

The dimensionless system of equations is

$$\Delta \mathbf{u} - \nabla p + \beta \nabla \cdot \mathbf{C} = 0, \quad (\text{S14})$$

$$\nabla \cdot \mathbf{u} = 0 \quad (\text{S15})$$

$$\frac{D\mathbf{C}}{Dt} = \text{Wi}^{-1} \mathbf{I} + (\nabla \mathbf{u} \mathbf{C} + \mathbf{C} \nabla \mathbf{u}^T) - \text{Wi}^{-1} \mathbf{C}, \quad (\text{S16})$$

for \mathbf{u} the fluid velocity, p the fluid pressure, and \mathbf{C} , the conformation tensor, a macroscopic average of the polymer orientation and stretching that is related to the polymer stress tensor by $\boldsymbol{\sigma}^p = \beta(\mathbf{C} - \mathbf{I})$. The boundary conditions are $\mathbf{u} = 0$ on the cylinder surface, and $\mathbf{u} = \mathbf{e}_x$ at infinity. the net force on the cylinder is

$$\mathbf{F} = \int_{\partial\Omega} (\boldsymbol{\sigma}^n + \beta \mathbf{C}) \cdot \mathbf{n} dS, \quad (\text{S17})$$

where $\boldsymbol{\sigma}^n$ is the Newtonian stress.

Expanding the solution in powers of β , Eqs. (S14)–(S16) at leading order are

$$\Delta \mathbf{u}_0 - \nabla p_0 = 0, \quad (\text{S18})$$

$$\nabla \cdot \mathbf{u}_0 = 0, \quad (\text{S19})$$

$$\frac{D\mathbf{C}_0}{Dt} = \text{Wi}^{-1} \mathbf{I} + (\nabla \mathbf{u}_0 \mathbf{C}_0 + \mathbf{C}_0 \nabla \mathbf{u}_0^T) - \text{Wi}^{-1} \mathbf{C}_0. \quad (\text{S20})$$

At first order the velocity and pressure satisfy

$$\Delta \mathbf{u}_1 - \nabla p_1 = -\nabla \cdot \mathbf{C}_0. \quad (\text{S21})$$

$$\nabla \cdot \mathbf{u}_1 = 0. \quad (\text{S22})$$

The force on the cylinder has the expansion

$$\mathbf{F} \sim \int_{\partial\Omega} \boldsymbol{\sigma}_0^n \cdot \mathbf{n} + \beta(\boldsymbol{\sigma}_1^n + \mathbf{C}_0) \cdot \mathbf{n} + \dots dS = \mathbf{F}_0 + \beta \mathbf{F}_1 + \dots. \quad (\text{S23})$$

From this expression, it appears the velocity and pressure are needed at first order to get the force at first order. However, using the reciprocal relation the first order force can be obtained from the leading order solution.

To use the reciprocal relation from Eq. (S13), we make the choice

$$\mathbf{u} = \mathbf{u}_0 - \mathbf{e}_x \quad (\text{S24})$$

$$\mathbf{u}' = \mathbf{u}_1 \quad (\text{S25})$$

and from Eqns. (S18) and (S21), the respective stresses satisfy

$$\nabla \cdot \boldsymbol{\sigma} = 0 \quad (\text{S26})$$

$$\nabla \cdot \boldsymbol{\sigma}' = -\nabla \cdot \mathbf{C}_0. \quad (\text{S27})$$

Plugging these into the reciprocal relation, Eq. (S13), gives

$$-(\mathbf{u}_0 - \mathbf{e}_x) \cdot \nabla \cdot \mathbf{C}_0 = \nabla \cdot ((\mathbf{u}_0 - \mathbf{e}_x) \cdot \boldsymbol{\sigma}_1^n - \mathbf{u}_1 \cdot \boldsymbol{\sigma}_0^n) \quad (\text{S28})$$

Because \mathbf{e}_x is constant, the above equation can be rearranged to

$$-\mathbf{u}_0 \cdot \nabla \cdot \mathbf{C}_0 = \nabla \cdot (\mathbf{u}_0 \cdot \boldsymbol{\sigma}_1^n - \mathbf{e}_x \cdot (\boldsymbol{\sigma}_1^n + \mathbf{C}_0) - \mathbf{u}_1 \cdot \boldsymbol{\sigma}_0^n). \quad (\text{S29})$$

Now integrate the above expression, apply the divergence theorem, use that $\mathbf{u}_0 = \mathbf{u}_1 = 0$ on the surface and that the stresses are zero at infinity to get

$$\int_{\Omega} -\mathbf{u}_0 \cdot \nabla \cdot \mathbf{C}_0 dV = \int_{\partial\Omega} \mathbf{e}_x \cdot (\boldsymbol{\sigma}_1^n + \mathbf{C}_0) \cdot \mathbf{n} dS = \mathbf{e}_x \cdot \mathbf{F}_1. \quad (\text{S30})$$

Finally, integrate the left side by parts and use that $\mathbf{u}_0 = 0$ on the surface to get

$$\mathbf{e}_x \cdot \mathbf{F}_1 = \int_{\Omega} \nabla \mathbf{u}_0 : \mathbf{C}_0 dV. \quad (\text{S31})$$

This gives an expression for the force at first order in terms of leading order quantities. We can manipulate this further using the equation for the conformation tensor. The polymer strain energy is $\mathcal{E} = \int_{\Omega} \text{Tr}(\mathbf{C} - \mathbf{I}) dV$. By taking the trace of Eqn. (S20), the equation for the strain energy at leading order is

$$\frac{d}{dt} \mathcal{E}_0 = 2 \int_{\Omega} \frac{\partial (u_0)_i}{\partial x_j} (C_0)_{ij} dV - \text{Wi}^{-1} \mathcal{E}_0. \quad (\text{S32})$$

Taking this equation at steady state, and combining it with Eqn. (S31) gives the expression for the force in terms of the strain energy as

$$\mathbf{e}_x \cdot \mathbf{F}_1 = \frac{1}{2\text{Wi}} \int_{\Omega} \text{Tr}(\mathbf{C}_0 - \mathbf{I}) dV. \quad (\text{S33})$$

References

- [1] A Acharya, RA Mashelkar, and J Ulbrecht. Flow of inelastic and viscoelastic fluids past a sphere. *Rheologica Acta*, 15(9):454–470, 1976.
- [2] MA Alves, FT Pinho, and PJ Oliveira. The flow of viscoelastic fluids past a cylinder: finite-volume high-resolution methods. *Journal of Non-Newtonian Fluid Mechanics*, 97(2-3):207–232, 2001.
- [3] Mark T Arigo and Gareth H McKinley. An experimental investigation of negative wakes behind spheres settling in a shear-thinning viscoelastic fluid. *Rheologica Acta*, 37(4):307–327, 1998.
- [4] Robert Byron Bird, Robert Calvin Armstrong, Ole Hassager, and Charles F Curtiss. *Dynamics of polymeric liquids*, volume 1. Wiley New York, 1977.
- [5] T. K. Chaudhury. On swimming in a visco-elastic liquid. *Journal of Fluid Mechanics*, 95(1):189–197, 1979.
- [6] K Chiba, Ki-Won Song, and A Horikawa. Motion of a slender body in quiescent polymer solutions. *Rheologica acta*, 25(4):380–388, 1986.
- [7] Ricardo Cortez. The method of regularized stokeslets. *SIAM Journal on Scientific Computing*, 23(4):1204–1225, 2001.
- [8] Ricardo Cortez, Lisa Fauci, and Alexei Medovikov. The method of regularized stokeslets in three dimensions: analysis, validation, and application to helical swimming. *Physics of Fluids*, 17(3):031504, 2005.
- [9] Vivekanand Dabade, Navaneeth K Marath, and Ganesh Subramanian. Effects of inertia and viscoelasticity on sedimenting anisotropic particles. *Journal of Fluid Mechanics*, 778:133–188, 2015.
- [10] Moumita Dasgupta, Bin Liu, Henry C Fu, Michael Berhanu, Kenneth S Breuer, Thomas R Powers, and Arshad Kudrolli. Speed of a swimming sheet in Newtonian and viscoelastic fluids. *Physical Review E*, 87(1):13015, 2013.
- [11] Gwynn J Elfring. A note on the reciprocal theorem for the swimming of simple bodies. *Physics of Fluids*, 27(2):023101, 2015.
- [12] Gwynn J Elfring and Gaurav Goyal. The effect of gait on swimming in viscoelastic fluids. *Journal of Non-Newtonian Fluid Mechanics*, 234:8–14, 2016.
- [13] Julian Espinosa-Garcia, Eric Lauga, and Roberto Zenit. Fluid elasticity increases the locomotion of flexible swimmers. *Physics of Fluids (1994-present)*, 25(3):031701, 2013.
- [14] Henry C Fu, Thomas R Powers, and Charles W Wolgemuth. Theory of swimming filaments in viscoelastic media. *Physical review letters*, 99(25):258101, 2007.
- [15] Henry C Fu, Charles W Wolgemuth, and Thomas R Powers. Beating patterns of filaments in viscoelastic fluids. *Physical Review E*, 78(4):041913, 2008.
- [16] Henry C Fu, Charles W Wolgemuth, and Thomas R Powers. Swimming speeds of filaments in nonlinearly viscoelastic fluids. *Physics of Fluids (1994-present)*, 21(3):033102, 2009.

- [17] Glenn R Fulford, David F Katz, and Robert L Powell. Swimming of spermatozoa in a linear viscoelastic fluid. *Biorheology*, 35(4):295–309, 1998.
- [18] Giovanni P Galdi. Slow steady fall of rigid bodies in a second-order fluid. *Journal of non-newtonian fluid mechanics*, 90(1):81–89, 2000.
- [19] James Gray and GJ Hancock. The propulsion of sea-urchin spermatozoa. *Journal of Experimental Biology*, 32(4):802–814, 1955.
- [20] GJ Hancock. The self-propulsion of microscopic organisms through liquids. *Proceedings of the Royal Society of London A: Mathematical, Physical and Engineering Sciences*, 217(1128):96–121, 1953.
- [21] John Happel and Howard Brenner. *Low Reynolds number hydrodynamics: with special applications to particulate media*, volume 1. Springer Science & Business Media, 2012.
- [22] Howard H Hu and Daniel D Joseph. Numerical simulation of viscoelastic flow past a cylinder. *Journal of Non-Newtonian Fluid Mechanics*, 37(2-3):347–377, 1990.
- [23] PY Huang, Howard H Hu, and Daniel D Joseph. Direct simulation of the sedimentation of elliptic particles in oldroyd-b fluids. *Journal of Fluid Mechanics*, 362:297–326, 1998.
- [24] RE Johnson and CJ Brokaw. Flagellar hydrodynamics. a comparison between resistive-force theory and slender-body theory. *Biophysical journal*, 25(1):113–127, 1979.
- [25] Robert E Johnson. An improved slender-body theory for stokes flow. *Journal of Fluid Mechanics*, 99(2):411–431, 1980.
- [26] DD Joseph. Flow induced microstructure in newtonian and viscoelastic fluids. *UMSI research report/University of Minnesota (Minneapolis, Mn). Supercomputer institute*, 99:97, 1996.
- [27] Joseph B Keller and Sol I Rubinow. Slender-body theory for slow viscous flow. *Journal of Fluid Mechanics*, 75(4):705–714, 1976.
- [28] Sangtae Kim. The motion of ellipsoids in a second order fluid. *Journal of non-newtonian fluid mechanics*, 21(2):255–269, 1986.
- [29] Eric Lauga. Propulsion in a viscoelastic fluid. *Phys. Fluids*, 19(8):83104, 2007.
- [30] L Gary Leal. The motion of small particles in non-newtonian fluids. *Journal of Non-Newtonian Fluid Mechanics*, 5:33–78, 1979.
- [31] LG Leal. The slow motion of slender rod-like particles in a second-order fluid. *Journal of Fluid Mechanics*, 69(2):305–337, 1975.
- [32] Chuanbin Li, Boyang Qin, Arvind Gopinath, Paulo E Arratia, Becca Thomases, and Robert D Guy. Flagellar swimming in viscoelastic fluids: role of fluid elastic stress revealed by simulations based on experimental data. *Journal of The Royal Society Interface*, 14(135):20170289, 2017.
- [33] James Lighthill. Flagellar hydrodynamics. *SIAM review*, 18(2):161–230, 1976.
- [34] Bin Liu, Thomas R Powers, and Kenneth S Breuer. Force-free swimming of a model helical flagellum in viscoelastic fluids. *Proceedings of the National Academy of Sciences*, 108(49):19516–19520, 2011.

- [35] Gareth H McKinley, Robert C Armstrong, and Robert Brown. The wake instability in viscoelastic flow past confined circular cylinders. *Phil. Trans. R. Soc. Lond. A*, 344(1671):265–304, 1993.
- [36] Matthew NJ Moore and Michael J Shelley. A weak-coupling expansion for viscoelastic fluids applied to dynamic settling of a body. *Journal of Non-Newtonian Fluid Mechanics*, 183:25–36, 2012.
- [37] Constantine Pozrikidis. *Boundary integral and singularity methods for linearized viscous flow*. Cambridge University Press, 1992.
- [38] Boyang Qin, Arvind Gopinath, Jing Yang, Jerry P Gollub, and Paulo E Arratia. Flagellar kinematics and swimming of algal cells in viscoelastic fluids. *Scientific reports*, 5:9190, 2015.
- [39] Michael Renardy. Asymptotic structure of the stress field in flow past a cylinder at high weissenberg number. *Journal of non-newtonian fluid mechanics*, 90(1):13–23, 2000.
- [40] Emily E Riley and Eric Lauga. Enhanced active swimming in viscoelastic fluids. *EPL (Europhysics Letters)*, 108(3):34003, 2014.
- [41] Daniel Salazar, Alexandre M. Roma, and Hector D. Ceniceros. Numerical study of an inextensible, finite swimmer in stokesian viscoelastic flow. *Physics of Fluids*, 28(6):063101, 2016.
- [42] XN Shen and Paulo E Arratia. Undulatory swimming in viscoelastic fluids. *Physical review letters*, 106(20):208101, 2011.
- [43] Saverio E Spagnolie, Bin Liu, and Thomas R Powers. Locomotion of helical bodies in viscoelastic fluids: enhanced swimming at large helical amplitudes. *Physical review letters*, 111(6):068101, 2013.
- [44] Howard A Stone and Aravinthan DT Samuel. Propulsion of microorganisms by surface distortions. *Physical review letters*, 77(19):4102, 1996.
- [45] Joseph Teran, Lisa Fauci, and Michael Shelley. Viscoelastic fluid response can increase the speed and efficiency of a free swimmer. *Physical review letters*, 104(3):038101, 2010.
- [46] Becca Thomases and Robert D Guy. Mechanisms of elastic enhancement and hindrance for finite-length undulatory swimmers in viscoelastic fluids. *Physical review letters*, 113(9):098102, 2014.
- [47] Becca Thomases and Robert D Guy. The role of body flexibility in stroke enhancements for finite-length undulatory swimmers in viscoelastic fluids. *Journal of Fluid Mechanics*, 825:109–132, 2017.
- [48] P Wapperom and M Renardy. Numerical prediction of the boundary layers in the flow around a cylinder using a fixed velocity field. *Journal of non-newtonian fluid mechanics*, 125(1):35–48, 2005.
- [49] R Byron Bird, Robert C Armstrong, and Ole Hassager. Dynamics of polymeric liquids. volume 1: fluid mechanics. *A Wiley-Interscience Publication, John Wiley & Sons*, 1987.
- [50] OG Harlen. High-deborah-number flow of a dilute polymer solution past a sphere falling along the axis of a cylindrical tube. *Journal of Non-Newtonian Fluid Mechanics*, 37(2-3):157–173, 1990.

- [51] OG Harlen, JM Rallison, and MD Chilcott. High-deborah-number flows of dilute polymer solutions. *Journal of Non-Newtonian Fluid Mechanics*, 34(3):319–349, 1990.
- [52] Donald L Koch, Eric F Lee, and Ibrahim Mustafa. Stress in a dilute suspension of spheres in a dilute polymer solution subject to simple shear flow at finite deborah numbers. *Physical Review Fluids*, 1(1):013301, 2016.
- [53] Robert G Owens and Timothy N Phillips. *Computational rheology*. World Scientific, 2002.
- [54] JM Rallison and EJ Hinch. Do we understand the physics in the constitutive equation? *Journal of Non-Newtonian Fluid Mechanics*, 29:37–55, 1988.
- [55] Rossella Scirocco, Jan Vermant, and Jan Mewis. Shear thickening in filled boger fluids. *Journal of rheology*, 49(2):551–567, 2005.
- [56] Becca Thomases and Michael Shelley. Emergence of singular structures in Oldroyd-B fluids. *Physics of fluids*, 19(10):103103, 2007.
- [57] Michael Renardy. A comment on smoothness of viscoelastic stresses. *Journal of non-newtonian fluid mechanics*, 138(2):204–205, 2006.
- [58] Ronald G Larson. The structure and rheology of complex fluids (topics in chemical engineering). *Oxford University Press, New York, Oxford*, 86:108, 1999.